Chemical Science

ROYAL SOCIETY OF CHEMISTRY

EDGE ARTICLE

View Article Online
View Journal | View Issue

Cite this: *Chem. Sci.*, 2022, **13**, 10815

All publication charges for this article have been paid for by the Royal Society of Chemistry

Received 16th June 2022
Accepted 16th August 2022

DOI: 10.1039/d2sc03365h

rsc.li/chemical-science

An excipient-free "sugar-coated bullet" for the targeted treatment of orthotopic hepatocellular carcinoma†

Feiyang Liu,[a] Lingyan Liu,[b] Dongya Liu,[a] Peng Wei, *[b] Wei Feng [a] and Tao Yi *[ab]

Several components of traditional nanoformulations that result in structural heterogeneity, poor reproducibility, excipient-trigged biotoxicity, and low retention of antitumor drugs in neoplastic foci are important barriers limiting clinical translation. We report an excipient-free nanoformulation prepared by a reactive oxygen species (ROS)-responsive amphiphilic prodrug (**Gal-MB-DOX**) for the targeted treatment of orthotopic hepatocellular carcinoma (HCC). **Gal-MB-DOX** can form monocomponent nanoparticles with a galactose-rich surface similar to a "sugar-coated bullet" through self-assembly in aqueous solution. This nanoformulation can be decomposed quickly by ROS and release free hydrophobic drugs that further precipitate into larger particles, potentially promoting the retention of drugs in tumor cells. These sugar-coated bullets selectively target tumor cells through passive and active targeting, resulting in high *in vivo* therapeutic efficacy in an orthotopic HCC mouse model. This monocomponent nanomedicine system provides a simple but effective strategy for the treatment of tumors.

1 Introduction

Nanomedicine provides a promising opportunity to improve the clinical outcomes of traditional chemotherapeutics that often suffer from the drawbacks of poor water solubility, low tumor-targeting ability, and rapid blood/renal clearance.[1–3] Some nanoformulations, including liposomes,[4–7] polymers.[8–11] and inorganic materials[12–14] that possess enhanced permeability and retention (EPR) effect show greater efficacy than free molecular drugs in the laboratory. However, few anticancer nanodrugs are approved by the food and drug administration (FDA).[15–17] One of the most obvious limitations is that multiple components are often required for those nanoformulations, which results in structural heterogeneity, poor reproducibility, and excipient-trigged biotoxicity, which are important barriers limiting clinical translation.[18–20] Another limitation is the low retention of antitumor drugs in neoplastic foci despite their transport to the tumor with the assistance of nanocarriers.[21–23] The molecular drugs are pumped out by efflux proteins in cancer cells, leading to a low drug concentration in the tumor and thus decreased pharmaceutical efficacy.[24–26]

In light of the current challenges in nanomedicine, alternative strategies involving the fabrication of monocomponent nanoformulations[27–31] with a size aggregation effect after activation in the tumor microenvironment (TME)[32,33] are highly attractive for oncotherapy and clinical translation. TME-responsive small-molecule prodrugs possessing single and clear structure are the ideal candidates for the construction of monocomponent nanoformulations because their distinct advantages such as simple but reproducible preparation and negligible excipient-derived biotoxicity.[34,35] We have developed some stimuli-responsive or size transformed systems for biological detection and disease theranostics in the past few years.[33,36–40] Particularly, we recently constructed a platform that could quickly (seconds level response time) release amino compounds conjugated to leucomethylene (LMB) through an urea bond when stimulated with HOCl (Fig. 1A).[41] To further develop a multifunctional molecular prodrug system that could effectively form monocomponent nanoparticles (NPs), in the present study we introduced an arylamine building block 2,6-bis (hydroxymethyl) aniline (BHA) into the LMB-based amino release system to obtain a multiple reactive oxygen species (ROS)-responsive theranostic molecular platform. The benzyl alcohols of BHA are flexible chemical reaction sites that can conjugate with various molecules such as target ligands or molecular drugs. Removal of LMB by ROS activated a cascade reaction on BHA, and the active payloads on two hydroxyl groups were ultimately released.[42–45] Furthermore, LMB could

[a]*Department of Chemistry, Fudan University, Shanghai 200438, China*

[b]*State Key Laboratory for Modification of Chemical Fibers and Polymer Materials, Shanghai Engineering Research Center of Nano-Biomaterials and Regenerative Medicine, College of Chemistry, Donghua University, Chemical Engineering and Biotechnology, Shanghai 201620, China. E-mail: yitao@dhu.edu.cn; weipeng@dhu.edu.cn*

† Electronic supplementary information (ESI) available: experimental details, synthesis and characterization of the prodrugs, additional figures and table. See https://doi.org/10.1039/d2sc03365h

be rapidly transformed to MB, which exhibited near-infrared (NIR) fluorescence emission (Fig. 1B).

To verify the effectiveness of this system for the treatment of tumors, we prepared the first example of an excipient-free nanoformulation that was self-assembled by a ROS-responsive molecular prodrug, **Gal-MB-DOX**, for the targeted treatment of orthotopic hepatocellular carcinoma (HCC) (Fig. 1C and D). In this prodrug, galactose served as a hydrophilic hepatocyte-targeting ligand that could specifically recognize the asialoglycoprotein receptor (ASGPR) overexpressed in liver cancer cells,[46–48] and DOX acts as a hydrophobic drug. The amphiphilic property of the prodrug allowed **Gal-MB-DOX** to self-assemble into monocomponent NPs similar to a "sugar-coated bullet" in aqueous solution. Upon ROS stimulation, this sugar-coated

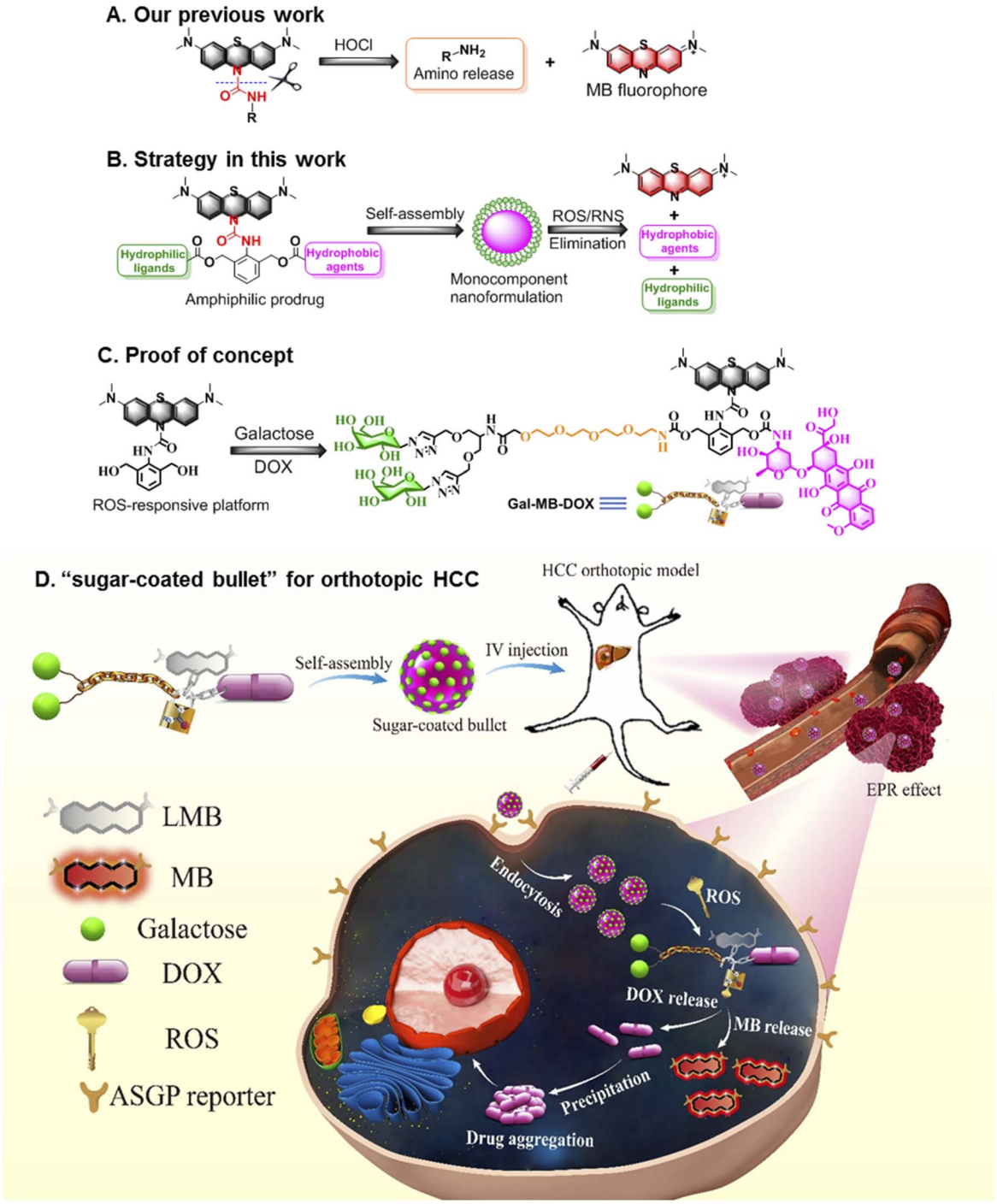

Fig. 1 The design strategy of this work. (A) Our previous work: amino release platform. (B) The strategy of this work. (C) Chemical structure of ROS-activated amphiphilic prodrug **Gal-MB-DOX**. (D) Schematic illustration of excipient-free "sugar-coated bullet" for the targeted treatment of orthotopic HCC.

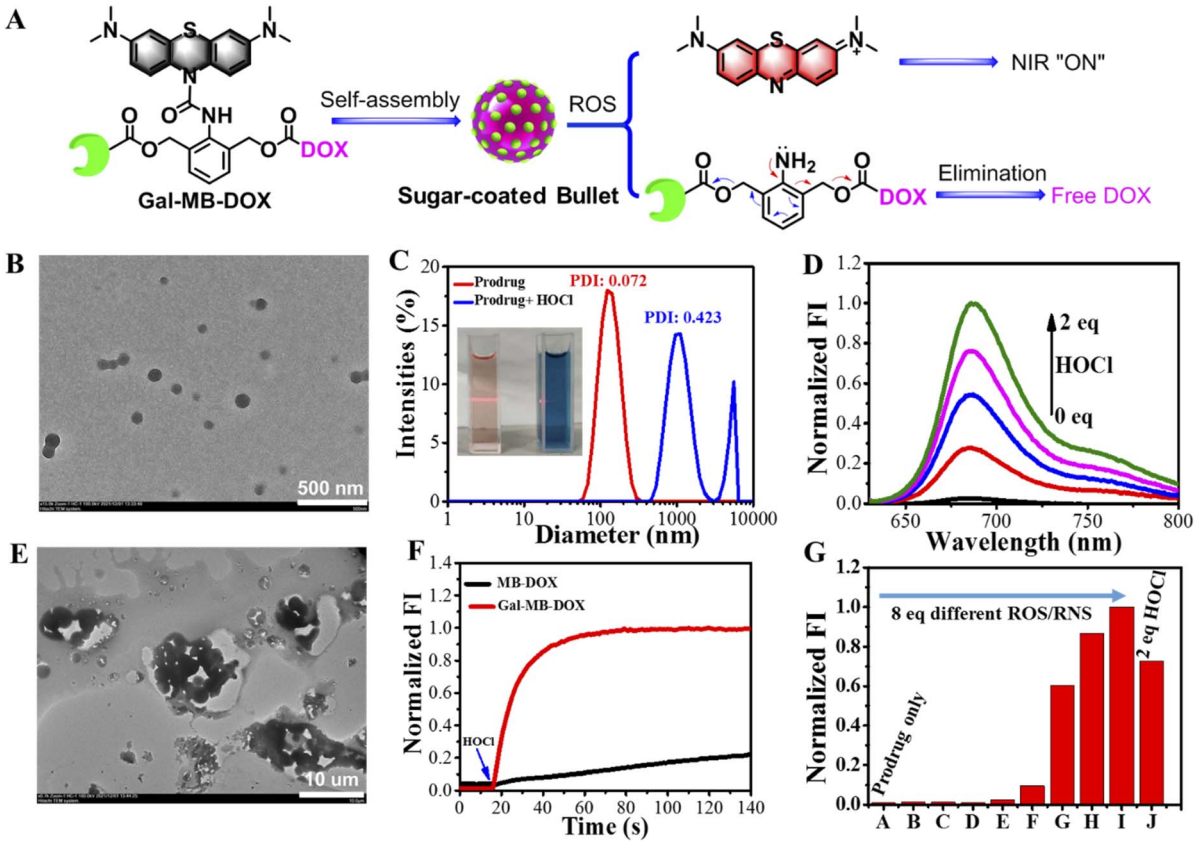

Fig. 2 Formation of the monocomponent NPs and their ROS-responsive performance *in vitro*. (A) Schematic illustration of the monocomponent prodrug nanosystem based on ROS-responsive molecular prodrug **Gal-MB-DOX**. TEM image of the NPs prepared by **Gal-MB-DOX** before (B) and after (E) treatment of HOCl. (C) DLS data of the NPs before (red) and after (blue) treatment of HOCl. Inset: Tyndall effect before (left) and after (right) treatment of HOCl. (D) Fluorescent spectra of **Gal-MB-DOX** (5 μM) before and after addition of different concentration of HOCl (0 to 10 μM). (F) Time-dependent fluorescent intensity of **Gal-MB-DOX** (5 μM) at 686 nm after adding HOCl (10 μM). (G) Fluorescence intensities of **Gal-MB-DOX** (5 μM) at 686 nm after adding various ROS/RNS (from B to I: H_2O_2, O_2^-, TBHP, ROO·, NO, *t*-BuOO·, ·OH, and $ONOO^-$ with concentrations of 40 μM, and J: HOCl with a concentration of 10 μM). The fluorescent spectra were recorded with $\lambda_{ex} = 620$ nm, in PB (10 mM, pH 7.4, 0.5% DMF).

bullet was quickly decomposed based on the cleavage of the urea bond in **Gal-MB-DOX**, leading to the release of MB and free DOX, which precipitated as larger particles, potentially promoting the retention of drugs in tumor cells. In addition, the NIR fluorescence of MB could be used as a signal for tracking the drug release process (Fig. 1D and 2A). To evaluate the therapeutic effect more realistically, an orthotopic HCC mouse model in which tumor cells grew in the liver was constructed.[49,50] The sugar-coated bullets selectively targeted the HCC cells through passive (EPR effect) and active (galactose) targeting after administration, and DOX was released in HCC, resulting in high *in vivo* therapeutic efficacy in an orthotopic HCC mouse model.

2 Results and discussion

2.1 Formation of the monocomponent NPs

The molecular prodrug **Gal-MB-DOX** and control compound **MB-DOX** without the targeted ligand galactose were synthesized according to Scheme S1–S3 (ESI†). Monocomponent NPs of **Gal-MB-DOX** were prepared in aqueous solution *via* a self-assembly process using a simple nanoprecipitation method (Fig. 2A). Transmission electron microscopy (TEM) images suggested that the NPs were monodispersed with a uniform spherical-like structure of approximately 110 nm in diameter (Fig. 2B). The Tyndall effect of **Gal-MB-DOX** in aqueous solution further confirmed the generation of nanospecies (Fig. 2C). The average hydrodynamic diameter of the NPs determined by dynamic light scattering (DLS) was 125.6 nm (Fig. 2C). These results suggest that **Gal-MB-DOX** could form an excipient-free nanoformulation by simple self-assembly.

2.2 ROS-responsive performance *in vitro*

The practicability of the nanoprodrug was next demonstrated by evaluating the ROS-responsive performance in phosphate buffer (PB, pH 7.4). As shown in Fig. 2C, treatment with HOCl caused an obvious color change from amaranth to blue, and the Tyndall effect subsequently disappeared. UV-visible absorption and fluorescence spectral changes of the prodrug (5 μM) demonstrated the rapid response activity towards HOCl (Fig. 2D, S1 and S2†). After the addition of HOCl, the absorption

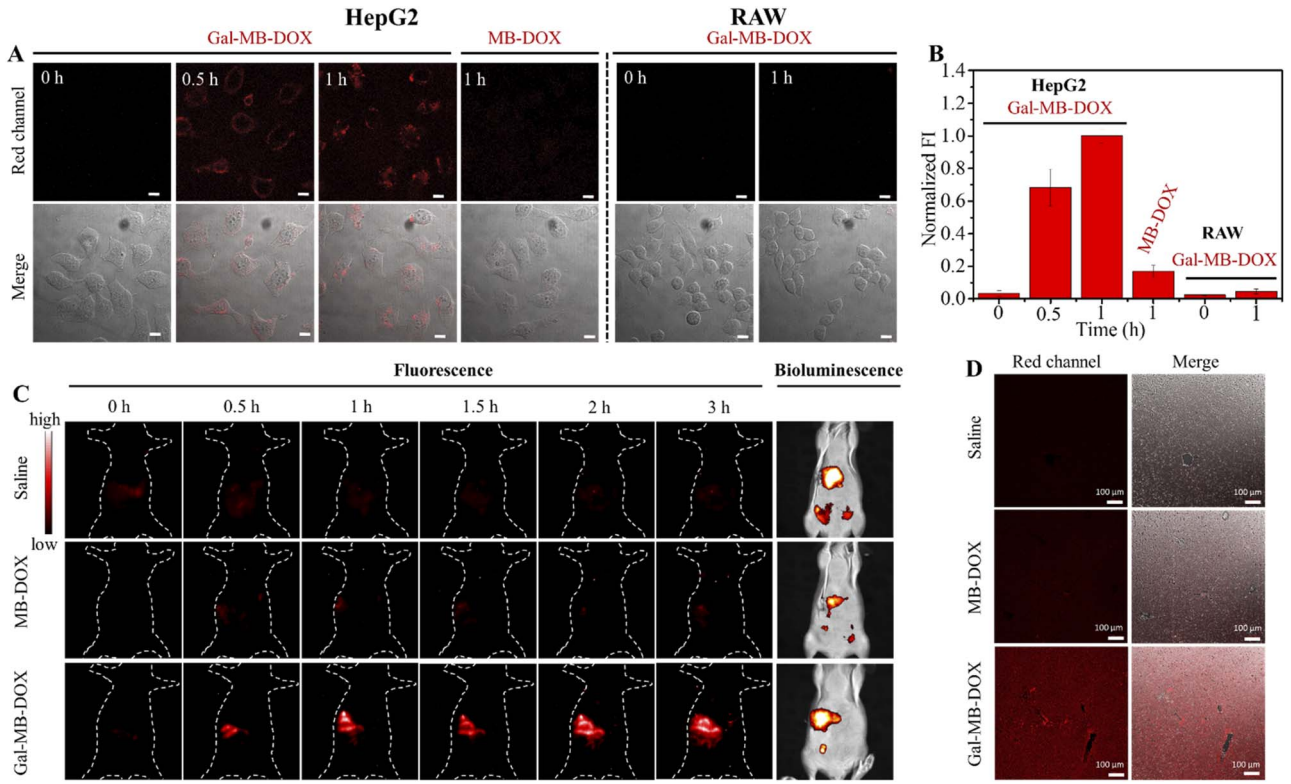

Fig. 3 Tumor targeting behavior of **Gal-MB-DOX** NPs. (A) CLSM images of prodrugs in HepG2 and RAW cells incubated with **Gal-MB-DOX** NPs (10 μM) or **MB-DOX** (10 μM) for different time. Red channel: 700 ± 50 nm, λ_{ex} = 633 nm. Scale bar = 20 μm. (B) The fluorescence intensity output in (A). (C) *In vivo* fluorescence and bioluminescence imaging of the orthotopic HCC model at different time after intravenous injection of (a) saline, (b) **MB-DOX** (1 mM, 100 μL) and (c) **Gal-MB-DOX** NPs (1 mM, 100 μL). White dotted line indicated the outline of mice. (D)The fluorescence images of excised liver tissues slices from the orthotopic HCC model injected with saline, **MB-DOX** (1 mM, 100 μL) and **Gal-MB-DOX** NPs (1 mM, 100 μL), respectively.

band at 664 nm and the emission at 686 nm corresponding to MB showed a HOCl concentration dependent increase with a low detection limit of 94.74 nM (Fig. S3†). Besides, the fluorescence signal at 686 nm quickly reached a plateau within only 30 s after addition of HOCl (10 μM), with an observed rate constant of 0.06402 s^{-1} under pseudo-first-order conditions, indicating the high sensitivity and quick reaction of **Gal-MB-DOX** toward HOCl (Fig. 2F). This suggested the activation of the prodrug by HOCl and the release of MB through urea bond cleavage (Scheme S4†). The accompanying NIR fluorescence of MB could be used as the signal to track the process of drug release. In addition, the increased fluorescence of the DOX channel and mass spectroscopic analysis indicated that DOX was released at a rate of 79.62% (Fig. S4–S6†). The DLS data and TEM images indicated that the NPs were transformed into larger aggregates with a micrometer level size (Fig. 2C and E), supporting the decomposition of **Gal-MB-DOX** NPs and the release of the insoluble DOX by HOCl, which was further precipitated in a hydrophilic environment (Fig. S7†).

Generally, the level of HOCl was closely related to that of myeloperoxidase, which may not be high enough in some cancer cells;[51,52] therefore, broad-spectrum ROS responses may be more favorable for enhanced bioavailability of ROS-activated prodrugs. We thus investigated the reaction activity of **Gal-MB-DOX** towards biologically relevant ROS/RNS. As shown in Fig. 2G and S8,† in addition to HOCl, other ROS including tertbutoxy radical, hydroxyl radical, and peroxynitrite anion could also activate the prodrugs, demonstrating that **Gal-MB-DOX** could serve as a broad-spectrum ROS-responsive prodrug with potential *in vivo* applications. In addition, it is important for a prodrug not to be interfered by the common substances in organisms, therefore, the selectivity of **Gal-MB-DOX** toward amino acids or ions were investigated. Fig. S9† showed that the prodrug could not be activated by dozens of common ions and amino acids, indicating the excellent selectivity of **Gal-MB-DOX**.

The optical and morphological stability of **Gal-MB-DOX** NPs in PBS, cell culture medium, and serum were studied by UV-visible absorption and DLS analysis (Fig. S10†). The absorption change at 664 nm from MB could follow the chemical decomposition of the prodrug. As shown in Fig. S10,† negligible absorption enhancement at 664 nm of **Gal-MB-DOX** NPs was observed within 48 h in different mediums. The absorption was only increased by addition of ROS. The DLS analysis gave the similar results. These data indicated the good optical and morphological stability of the prodrug over a period of 48 h.

2.3 Cellular uptake and activation

The performance of the nanoprodrug was next investigated in ASGP receptor-positive HepG2 and negative RAW cells. As shown in Fig. 3A and B, HepG2 cells treated with **Gal-MB-DOX**

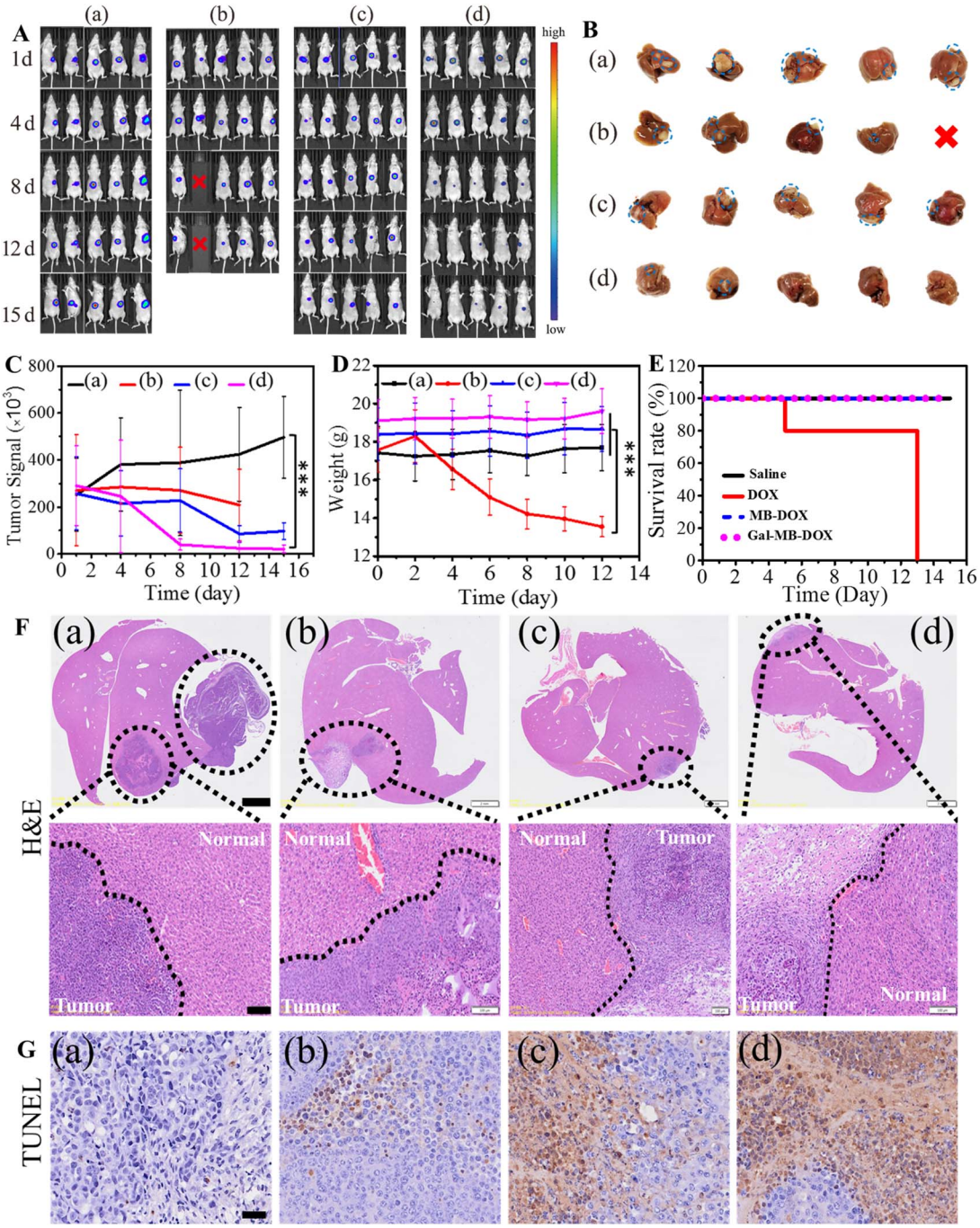

Fig. 4 *In vivo* antitumor performance in orthotopic HCC mouse models treated with (a) saline, (b) DOX, (c) **MB-DOX** and (d) **Gal-MB-DOX** NPs (0.2 mM, 100 μL). (A) Bioluminescence images and (C) intensity of the orthotopic HCC mice on days 1, 4, 8, 12 and 15 (Red cross indicated mice died, $n = 5$ biologically independent samples, data are presented as mean values ± SD. ***$p < 0.001$. (B) Photographs of excised liver tissues bearing tumor from each treatment group at the end of treatment, where the orthotopic tumor tissues were highlighted with blue dotted circles. (D) Body weight variations of the mice in various treatment groups within 15 days ($n = 5$). Data are presented as mean values ± SD. ***$p < 0.001$. (E) Survival rate of the mice within the treatment period from different treated groups. (F) H&E staining of liver slices from orthotopic HCC mice after treatments. Upper row: full scan of the liver organs, black circles indicate the tumors in liver, scale bars: 2 mm. Lower row: H&E staining of tumor sections, scale bars: 100 μm. (G) TUNEL staining of tumor sections after various treatments, scale bars: 50 μm.

NPs displayed time-dependent increased fluorescence signals from 0 to 60 min. However, a negligible fluorescence signal was observed in RAW cells under the same conditions. Flow cytometry analysis showed that the cellular uptake ratios of **Gal-MB-DOX** in HepG2 reached >90% at 15 min, which was considerably higher than that in RAW cells (31.6%) (Fig. S11†). In addition, the release of the DOX was completed within 1 h in HepG2 cells. However, **MB-DOX** lacking the galactose ligand displayed no significant fluorescence signal even after 60 min in HepG2 cells. These results demonstrated that the galactose

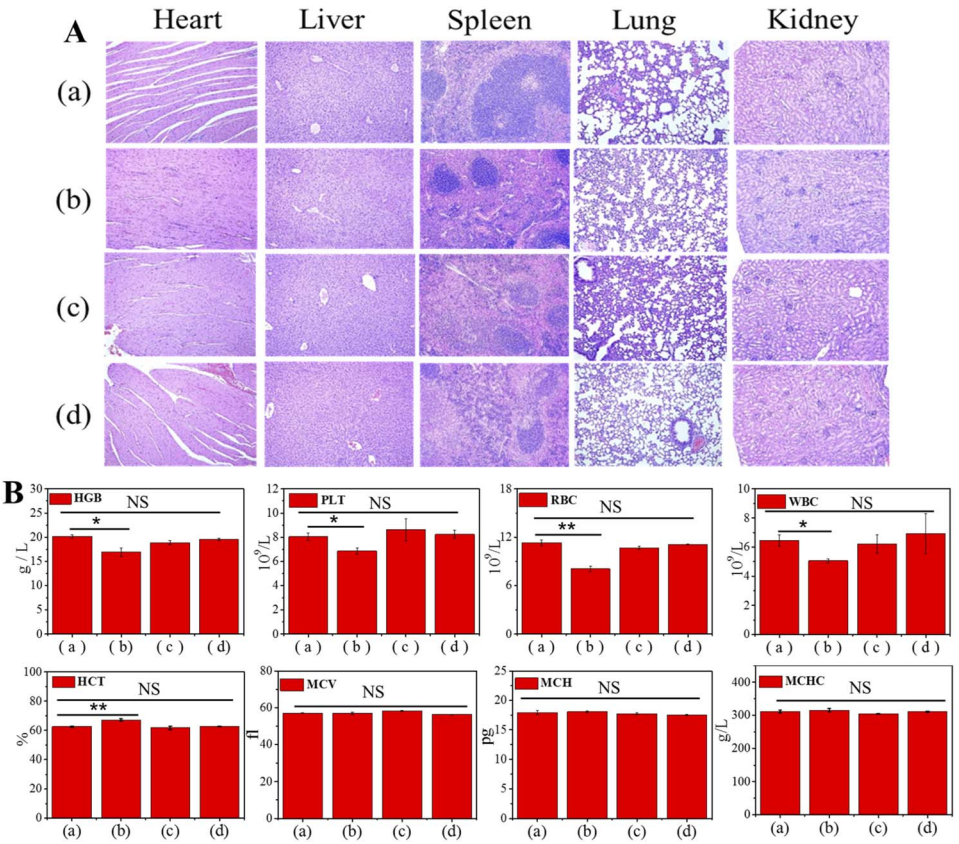

Fig. 5 Biosecurity evaluation of different treatments: (a) saline, (b) DOX, (c) MB-DOX and (d) Gal-MB-DOX. (A) H&E staining of the heart, liver, spleen, lung, and kidney of mice after 15 days of different treatments. Scale bar = 100 μm. (B) Blood routine analysis of healthy female F1 mice after intravenous injection with different treatments once every two days for one week (100 μL × 0.2 mM). These data are the mean ± sd; $n = 3$ independent experiments for red blood.

ligand facilitated the uptake of **Gal-MB-DOX** NPs by HepG2 cells and activation by the endogenous ROS/RNS.

We next investigated the cytotoxicity of **Gal-MB-DOX** using CCK-8 assays. As shown in Fig. S12,† the cytotoxicity of **Gal-MB-DOX** in HepG2 cells showed a significant dose-dependent increase from 0 to 120 μM after 24 h of incubation. **MB-DOX** showed almost no cytotoxicity in HepG2 cells even at a high dose of 120 μM, which could be attributed to its poor targeting capability for liver cancer cells. Both **MB-DOX** and **Gal-MB-DOX** exhibited low cytotoxicity in RAW cells at a concentration of 80 μM, with >80% cell survival observed.

It has been reported that free DOX could enhance the expression of caspase-3 in HepG2 cells, which leads to cell death by the induction of apoptosis.[24,53] The detection of caspase-3 activity in HepG2 cells was performed to further demonstrate the cytotoxicity of **Gal-MB-DOX**. As shown in Fig. S13,† the fluorescence intensity indicating the expression of caspase-3 enhanced with the increased concentration of **Gal-MB-DOX**, indicating that the prodrug could cause the apoptosis induced cell death through the release of DOX in HepG2 cells. Moreover, the treatment of caspase-3 inhibitor (Ac-DEVD-CHO, 20 μM) significantly reduced the caspase-3 expression in **Gal-MB-DOX** group (200 μM) but did not affect cells without **Gal-MB-DOX** treated. The results further corroborated the specific cytotoxicity of **Gal-MB-DOX** for HepG2 cells, consistent with those of fluorescence imaging (Fig. 3A). These data indicate that **Gal-MB-DOX** is an ideal candidate for liver cancer treatment *in vivo*.

2.4 *In vivo* biodistribution

Balb/c mice were surgically implanted with tumor tissue (1–2 mm^3) from HepG2-Luc cells to construct an orthotopic HCC model. The orthotopic xenograft model in which the tumor cells grew in the liver was a more realistic model of a natural tumor than the subcutaneous model. The tumor location could be determined by detecting the bioluminescence signal from the luciferase of implanted tumor cells. The target activation and biodistribution of the prodrugs were first investigated. As shown in Fig. 3C, intravenous injection of **Gal-MB-DOX** NPs (0.2 mM, 100 μL) caused a time-dependent increase in the fluorescence signal in the liver tumor region of mice up to 3 h. The signal co-localized with the bioluminescence signal from the implanted HepG2-Luc cells, indicating effective liver targeting and activation of **Gal-MB-DOX** NPs. Negligible fluorescence signals in the tumor region were observed in the saline and **MB-DOX** groups (0.2 mM, 100 μL). At 3 h after injection, the major organs of mice were harvested for *ex vivo* imaging (Fig. S14†). Compared with the saline and **MB-DOX** groups, an enhanced fluorescence signal was observed in the liver and

mainly concentrated in the tumor area in the **Gal-MB-DOX** NPs group. The *ex vivo* imaging of the excised liver tissues slices from the orthotopic HCC model of different groups was then performed (Fig. 3D). Much stronger red fluorescence signal was seen in **Gal-MB-DOX** NPs group than other two groups, demonstrating the activation of the liver tumor-targeting ability of **Gal-MB-DOX** NPs.

2.5 *In vivo* antitumor effect

Next, the antitumor effect of **Gal-MB-DOX** NPs was evaluated in the orthotopic HCC model. The orthotopic tumor-bearing mice were randomly divided into four groups ($n = 5$ per group): (a) saline, (b) DOX, (c) **MB-DOX** and (d) **Gal-MB-DOX** NPs. The treatment was implemented by intravenously injecting with saline, free DOX, **MB-DOX** and **Gal-MB-DOX** NPs every two days (0.2 mM, 100 μL) in a period of 15 day, and *in vivo* bioluminescence imaging was performed after each treatment. As shown in Fig. 4A, B and C, the highest therapeutic efficacy among the four groups was observed in the **Gal-MB-DOX** NPs group. Although DOX is a traditional antitumor drug, all mice treated with DOX died within 13 days because of the strong side effects (Fig. 4D and E). The survival time of the DOX-treated group was even shorter than that of the saline-treated group, indicating that the mice died from side effects rather than the tumor. However, all of the mice in prodrug-treated groups (**MB-DOX** and **Gal-MB-DOX** NPs) survived until the end of the study (16 days), verifying the advantage of the activated prodrugs.

Analysis of the excised liver organs harvested at the end of treatment confirmed the excellent antitumor effect of **Gal-MB-DOX** NPs, which resulted in a negligible tumor mass in the liver (Fig. 4B and F). Besides, the H&E staining of tumor sections showed apparent apoptosis in **MB-DOX** and **Gal-MB-DOX** NPs treated groups and no damage in normal liver tissue, indicating the biosecurity of the prodrugs (Fig. 4F). From TUNEL staining of the slices of tumor, abundant apoptosis in **MB-DOX** and **Gal-MB-DOX** NPs treated groups could be seen and tumor cell apoptosis was most notable in the **Gal-MB-DOX** NPs group further demonstrating the antitumor effect of the prodrugs (Fig. 4G). Routine blood analyses and H&E staining of major organs were performed at the end of therapy to evaluate the safety of the preparation (Fig. 5, S15†). Consistent with the body weight measurements (Fig. 4D), abnormal blood biochemical indexes were only observed in the DOX group. The myocardial fibers of the DOX group were thin and slightly atrophied. Taken together, the results indicated that the monocomponent NPs based on **Gal-MB-DOX** were effective and showed good biocompatibility in orthotopic liver tumor.

3 Conclusions

In this paper we report the first example of an excipient-free nanoformulation to the best of our knowledge prepared by self-assembly of a ROS-responsive amphiphilic theranostic prodrug. The prodrug **Gal-MB-DOX** is designed based on the skeleton of LMB and BHA coupled through a urea bond for the targeted treatment of orthotopic HCC. **Gal-MB-DOX** NPs has certain stability in normal physiological condition, but is decomposed rapidly (<30 s) by ROS to release free hydrophobic drugs that precipitated as larger particles *in vitro*, promoting the retention of drugs in tumor cells. **Gal-MB-DOX** NPs with a galactose-rich surface similar to a "sugar-coated bullet" are more likely to be ingested by ASGP reporter-positive HepG2 cells, and are highly cytotoxic against tumor cells rather than normal cells. These sugar-coated bullets selectively target tumor cells through passive and active targeting mechanisms, and thus showed strong *in vivo* therapeutic efficacy in an orthotopic HCC mouse model.

Comparing with the recently published prodrugs based on different response substances (Table S1†), **Gal-MB-DOX** NP has following advantages: (1) single components, repeatable preparation and low toxicity to normal cells/organs; (2) rapid responsibility to ROS with high sensitivity and (3) *in situ* aggregation of the released free drug at the tumor site that ensures effective local drug concentration. The construction strategy of this monocomponent nanoformulation can be easily applied to the treatment of other tumors or diseases by changing the targeting group and the type of drugs. This monocomponent prodrug nanosystem thus provides a simple but effective strategy for the treatment of tumors.

Data availability

All the experimental data are put in ESI.†

Author contributions

Feiyang Liu: design of the project, synthetic work, preparation and characterization of the prodrugs *in vitro*, writing the first draft. Lingyan Liu: characterization of the prodrugs *in vitro* and *in vivo*. Dongya Liu: characterization of the prodrugs *in vitro*. Peng Wei, Wei Feng and Tao Yi: supervision and design of the project, review and editing of the manuscript.

Ethical statement

The handling and care of the animals conformed to the guidelines of current international laws and policies (National Institutes of Health Guide for the Care and Use of Laboratory Animals, Publication No. 85-23, 1985, revised 1996). All animal experiments were performed according to procedures approved by the Fudan University Committee on Animal Care and Use. All protocols for animal studies conformed to the Guide for the Care and Use of Laboratory Animals.

Conflicts of interest

The authors declare no competing financial interests.

Acknowledgements

This study was financially supported by the National Natural Science Foundation of China (21877013, 22177019, 22007012), Fundamental Research Funds for the Central Universities (2232021A-06), Shanghai Sailing Program (20YF1401100) and

Science and Technology Commission of Shanghai Municipality (20DZ2254900). We also thank Qiuwen Guo for graphics assistance.

Notes and references

1 S. Mura, J. Nicolas and P. Couvreur, *Nat. Mater.*, 2013, **12**, 991–1003.
2 W. Fan, B. Yung, P. Huang and X. Chen, *Chem. Rev.*, 2017, **117**, 13566–13638.
3 N. Singh, S. Son, J. An, I. Kim, M. Choi, N. Kong, W. Tao and J. S. Kim, *Chem. Soc. Rev.*, 2021, **50**, 12883–12896.
4 G. Wang, C. Zhang, Y. Jiang, Y. Song, J. Chen, Y. Sun, Q. Li, Z. Zhou, Y. Shen and P. Huang, *Adv. Funct. Mater.*, 2021, **31**, 2102786.
5 Z. Zhao, W. Wang, C. Li, Y. Zhang, T. Yu, R. Wu, J. Zhao, Z. Liu, J. Liu and H. Yu, *Adv. Funct. Mater.*, 2019, **29**, 1905013.
6 E. Rideau, R. Dimova, P. Schwille, F. R. Wurm and K. Landfester, *Chem. Soc. Rev.*, 2018, **47**, 8572–8610.
7 N. Duan, J. Li, S. Song, F. Wang, Y. Yang, D. Nie, C. Wang, Y. Sheng, Y. Tao, J. Gao, C. Xu, Y. Wei and Y. Gan, *Adv. Funct. Mater.*, 2021, **31**, 2100605.
8 D. W. Binzel, X. Li, N. Burns, E. Khan, W. J. Lee, L. C. Chen, S. Ellipilli, W. Miles, Y. S. Ho and P. Guo, *Chem. Rev.*, 2021, **121**, 7398–7467.
9 S. Zhang, S. Zhang, S. Luo and D. Wu, *Coord. Chem. Rev.*, 2021, **445**, 214059.
10 K. Haupt, P. X. Medina Rangel and B. T. S. Bui, *Chem. Rev.*, 2020, **120**, 9554–9582.
11 S. Lv, M. Sylvestre, A. N. Prossnitz, L. F. Yang and S. H. Pun, *Chem. Rev.*, 2021, **121**, 11653–11698.
12 M. A. Shahbazi, L. Faghfouri, M. P. A. Ferreira, P. Figueiredo, H. Maleki, F. Sefat, J. Hirvonen and H. A. Santos, *Chem. Soc. Rev.*, 2020, **49**, 1253–1321.
13 D. An, J. Fu, B. Zhang, N. Xie, G. Nie, H. Ågren, M. Qiu and H. Zhang, *Adv. Funct. Mater.*, 2021, **31**, 2101625.
14 G. Lin, R. A. Revia and M. Zhang, *Adv. Funct. Mater.*, 2021, **31**, 2007096.
15 C. M. Dawidczyk, C. Kim, J. H. Park, L. M. Russell, K. H. Lee, M. G. Pomper and P. C. Searson, *J. Controlled Release*, 2014, **187**, 133–144.
16 P. Grodzinski, M. Kircher, M. Goldberg and A. Gabizon, *ACS Nano*, 2019, **13**, 7370–7376.
17 Y. Min, J. M. Caster, M. J. Eblan and A. Z. Wang, *Chem. Rev.*, 2015, **115**, 11147–11190.
18 C. Luo, J. Sun, B. Sun and Z. He, *Trends Pharmacol. Sci.*, 2014, **35**, 556–566.
19 J. C. Leroux, *Angew. Chem., Int. Ed.*, 2017, **56**, 15170–15171.
20 J. Shi, P. W. Kantoff, R. Wooster and O. C. Farokhzad, *Nat. Rev. Cancer*, 2017, **17**, 20–37.
21 Y. Wang, J. Xie, J. Kang, W. Choi, P. Jangili, B. Zhang, N. Xie, G. Nie, J. He, H. Zhang, L. Liu and J. S. Kim, *Adv. Funct. Mater.*, 2020, **30**, 2003338.
22 Y. Qin, F. Tong, W. Zhang, Y. Zhou, S. He, R. Xie, T. Lei, Y. Wang, S. Peng, Z. Li, J. Leong, H. Gao and L. Lu, *Adv. Funct. Mater.*, 2021, **31**, 2104645.
23 H. Luo, L. Kong, F. Zhang, C. Huang, J. Chen, H. Zhang, H. Yu, S. Zheng, H. Xu, Y. Zhang, L. Deng, G. Chen, H. A. Santos and W. Cui, *Adv. Funct. Mater.*, 2021, **31**, 2101262.
24 A. Sharma, M.-G. Lee, H. Shi, M. Won, J. F. Arambula, J. L. Sessler, J. Y. Lee, S.-G. Chi and J. S. Kim, *Chem*, 2018, **4**, 2370–2383.
25 S. N. Aleksakhina, A. Kashyap and E. N. Imyanitov, *Biochim. Biophys. Acta, Rev. Cancer*, 2019, **1872**, 188310.
26 J. I. Fletcher, M. Haber, M. J. Henderson and M. D. Norris, *Nat. Rev. Cancer*, 2010, **10**, 147–156.
27 G. Li, B. Sun, Y. Li, C. Luo, Z. He and J. Sun, *Small*, 2021, **17**, 2101460.
28 K. Lin, Z. Ma, J. Li, M. Tang, A. Lindstrom, M. Ramachandran, S. Zhu, T. y. Lin, L. Zhang and Y. Li, *Adv. Funct. Mater.*, 2021, **31**, 2008460.
29 C. Yan, Z. Guo, Y. Shen, Y. Chen, H. Tian and W. H. Zhu, *Chem. Sci.*, 2018, **9**, 4959–4969.
30 N. Yu, T. Liu, X. Zhang, N. Gong, T. Ji, J. Chen, X. J. Liang, D. S. Kohane and S. Guo, *Nano Lett.*, 2020, **20**, 5465–5472.
31 L.-H. Liu and X.-Z. Zhang, *Prog. Mater. Sci.*, 2022, **125**, 100919.
32 S. Li, Y. Zhang, X. Liu, Y. Tian, Y. Cheng, L. Tang and H. Lin, *Theranostics*, 2022, **12**, 76–86.
33 D. Liu, L. Liu, F. Liu, M. Zhang, P. Wei and T. Yi, *Adv. Sci.*, 2021, **8**, 2100074.
34 R. Kumar, W. S. Shin, K. Sunwoo, W. Y. Kim, S. Koo, S. Bhuniya and J. S. Kim, *Chem. Soc. Rev.*, 2015, **44**, 6670–6683.
35 H. Wang, J. Chang, M. Shi, W. Pan, N. Li and B. Tang, *Angew. Chem., Int. Ed.*, 2019, **58**, 1057–1061.
36 X. Li, C. Cao, P. Wei, M. Xu, Z. Liu, L. Liu, Y. Zhong, R. Li, Y. Zhou and T. Yi, *ACS Appl. Mater. Interfaces*, 2019, **11**, 12327–12334.
37 P. Wei, L. Liu, W. Yuan, J. Yang, R. Li and T. Yi, *Sci. China Chem.*, 2020, **63**, 1153–1158.
38 L. Liu, L. Jiang, W. Yuan, Z. Liu, D. Liu, P. Wei, X. Zhang and T. Yi, *ACS Sens.*, 2020, **5**, 2457–2466.
39 L. Liu, P. Wei, W. Yuan, Z. Liu, F. Xue, X. Zhang and T. Yi, *Anal. Chem.*, 2020, **92**, 10971–10978.
40 P. Wei, W. Yuan, F. Xue, W. Zhou, R. Li, D. Zhang and T. Yi, *Chem. Sci.*, 2018, **9**, 495–501.
41 P. Wei, L. Liu, Y. Wen, G. Zhao, F. Xue, W. Yuan, R. Li, Y. Zhong, M. Zhang and T. Yi, *Angew. Chem., Int. Ed.*, 2019, **58**, 4547–4551.
42 A. Alouane, R. Labruere, T. Le Saux, F. Schmidt and L. Jullien, *Angew. Chem., Int. Ed.*, 2015, **54**, 7492–7509.
43 S. Gnaim and D. Shabat, *Acc. Chem. Res.*, 2014, **47**, 2970–2984.
44 K. Cai, X. He, Z. Song, Q. Yin, Y. Zhang, F. M. Uckun, C. Jiang and J. Cheng, *J. Am. Chem. Soc.*, 2015, **137**, 3458–3461.
45 L. Liu, F. Liu, D. Liu, W. Yuan, M. Zhang, P. Wei and T. Yi, *Angew. Chem., Int. Ed.*, 2022, e202116807.
46 Y. Fu, H. H. Han, J. Zhang, X. P. He, B. L. Feringa and H. Tian, *J. Am. Chem. Soc.*, 2018, **140**, 8671–8674.
47 M. Wang, Z. Li, F. Liu, Q. Yi, C. Pu, Y. Li, T. Luo, J. Liang and J. Wang, *J. Med. Chem.*, 2021, **64**, 14793–14808.

48 A. A. D'Souza and P. V. Devarajan, *J. Controlled Release*, 2015, **203**, 126–139.
49 J. Pan, Y. Xu, Q. Wu, P. Hu and J. Shi, *J. Am. Chem. Soc.*, 2021, **143**, 8116–8128.
50 K. Wang, F. M. Kievit, J. G. Sham, M. Jeon, Z. R. Stephen, A. Bakthavatsalam, J. O. Park and M. Zhang, *Small*, 2016, **12**, 477–487.
51 S. J. Klebanoff, *J. Leukocyte Biol.*, 2005, **77**, 598–625.
52 A. J. Kettle and C. C. Winterbourn, *Redox Rep.*, 1997, **3**, 3–15.
53 A. Sharma, E. Kim, S. Mum, M. S. Ji, B. G. Chung and J. S. Kim, *Dyes Pigm.*, 2019, **163**, 628–633.